Beam and Cantilever Supported PMUTs for Enhanced Transmit Sensitivity and Linearity

Shyam Trivedi[1]*, Duan Jian Goh[1], Prakasha Chigahalli Ramegowda[1], Jihang Liu[1], Yong Shun Teo[1], Hong Yan[1], Ravi Shankar[2], Naadaa Ghulaam Zakiyyan[2], Amal Das[2], Carla Lazzari[2], Alberto Leotti[2]†, Yul Koh[1]‡

[1]Institute of Microelectronics (IME), Agency for Science Technology and Research (A*STAR), Singapore
[2]STMicroelectronics, Singapore

Date of acceptance: 18/08/2025

Abstract

This paper introduces curved-beam (CB) and curved-cantilever (CC) piezoelectric micromachined ultrasonic transducers (PMUTs) using 30% scandium-doped aluminum nitride (ScAlN), comparing their performance with conventional (C-PMUT) in the 45–75 kHz range. The CC-PMUT and CB-PMUT designs incorporate 2 µm edge slits to achieve piston-mode vibration, significantly enhancing the effective vibration area to 65% and 60%, respectively, compared to 33% for C-PMUT. This structural design improves linearity, with CC-PMUT demonstrating minimal frequency sensitivity to DC bias (±40 V) at 2.5 Hz/V, and CB-PMUT (7.5 Hz/V) both outperforming C-PMUT (100 Hz/V). Under increasing AC voltage excitation, CC-PMUT exhibit exceptional linearity with minimal resonance variation, while C-PMUTs and CB-PMUTs show nonlinear behavior with increasing frequency and stiffening effects. C-PMUT display the highest non-linearity, with a duffing coefficient 2.5 times larger than CB-PMUT. The CB-PMUT exhibits the highest displacement sensitivity (1025 nm/V) compared to C-PMUT (825 nm/V) and CC-PMUT (610 nm/V). Despite its four-fold smaller area, the CB-PMUT generates comparable absolute pressure to the C-PMUT. Its exceptional normalized transmission pressure sensitivity of 77 dB SPL/V/mm^2 surpasses both C-PMUT (65 dB) and CC-PMUT (67 dB), making it the highest reported among PZT and ScAlN counterparts. C-PMUT demonstrate the highest receive sensitivity at 8.7 mV/Pa, followed by CB-PMUT at 4.2 mV/Pa and CC-PMUT at 3.3 mV/Pa. In pitch-catch experiments, CB-PMUT and C-PMUT detect signals up to 3.8 m and 4 m, respectively, while CC-PMUT reach 2.7 m (10 V_{pp}, 12 dB SNR threshold), demonstrating their potential for ultrasonic range-finding.

Keywords— AlN, Air-coupled, Cantilever, Beam, Linearity, PMUT, ScAlN, Sensitivity, Ultrasonic

*e-mail: trivedis@a-star.edu.sg
†e-mail: alberto.leotti@st.com
‡e-mail: koh_yul@a-star.edu.sg

1 Introduction

Micromachined Ultrasonic Transducers (MUTs) consist of a membrane suspended over a cavity or bulk substrate, operating in flexural vibration mode [1]. These transducers primarily utilize two mechanisms of operation: Capacitive MUTs (CMUTs), which generate ultrasonic waves in the surrounding medium through electrostatic actuation across a narrow gap [2], and Piezoelectric MUTs (PMUTs), which leverage the inverse piezoelectric effect to induce stress in a thin piezoelectric film leading to vibration when a voltage is applied across it [3]. MUTs facilitate streamlined integration into various applications and increasingly replace traditional bulk piezoelectric transducers. The bending motion of the membrane enhances impedance matching between the transducer and the acoustic medium, effectively eliminating the need for separate impedance-matching layers [4]. The compact design of MUTs enables them to generate the same pressure with lower actuation voltages, reducing both power consumption and manufacturing costs [5]. These advantages stem from mass production techniques that simplify electronic integration and allow for the creation of large transducer arrays, making them suitable for ranging and imaging [6].

In contrast to CMUTs, PMUTs can achieve similar sensitivity levels without the need for a DC voltage bias, which enhances their suitability for integration into wearable devices and consumer electronic applications. Their design enables larger membrane vibrations by eliminating the need for extremely narrow cavity gaps, which extends the linear operating range [7], making it more suitable for air-coupled applications. PMUTs can attain a high electromechanical coupling coefficient (k_t^2) without requiring submicron cavity gaps, which simplifies the fabrication process and enhances cost-effectiveness [8]. Additionally, CMUTs are prone to issues such as dielectric charging, non-linearity, pull-in voltages, and performance drift, which can affect their long-term reliability [9, 10, 11]. In recent years, PMUTs have expanded beyond just range-finding applications into a diverse array of fields.

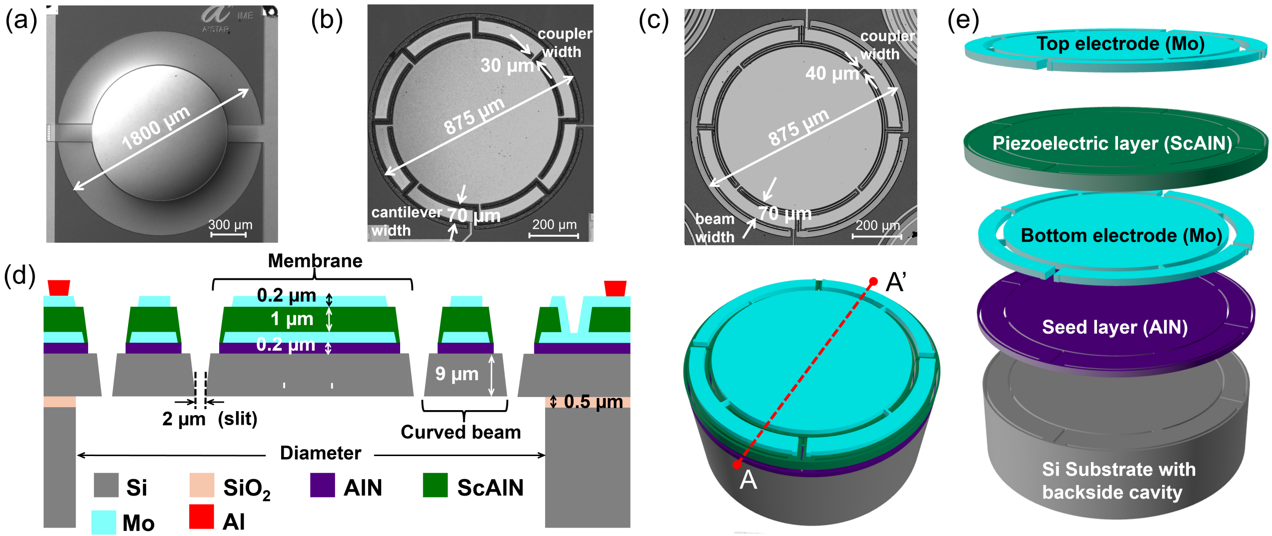

Figure 1: Optical microscope images of (a) conventional PMUT (C-PMUT), (b) curved-cantilever PMUT (CC-PMUT), and (c) curved-beam PMUT (CB-PMUT), with diameters, peripheral actuator widths, and coupler widths indicated. (d) Cross-sectional image of CB-PMUT along the line A-A' and (e) schematic exploded view showing the individual layers of the CB-PMUT design.

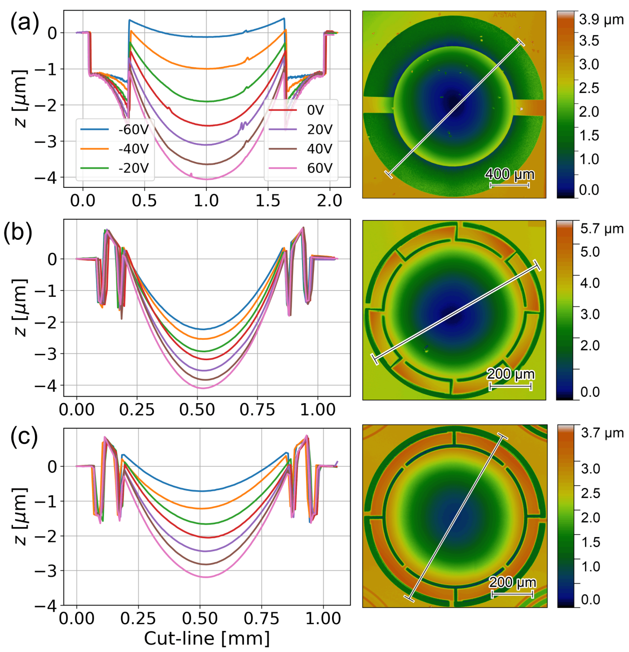

Figure 2: PMUT membrane top-view and line profile at different DC voltages for (a) C-PMUT, (b) CC-PMUT, and (c) CB-PMUT respectively.

Those based on Aluminum Nitride (AlN) or Scandium-doped Aluminum Nitride ($Sc_xAl_{1-x}N$) have seen growing adoption owing to their alignment with Complementary Metal-Oxide-Semiconductor(CMOS) based manufacturing standards, [12], making them increasingly relevant in medical imaging applications [13, 14] and diagnostics [15, 16]. Other areas where PMUTs are making significant inroads include mid-air haptic feedback for touch interfaces [17], gesture recognition [8], proximity and obstacle sensors for human-machine safety [18, 19], wake-up receivers [20, 21], and fingerprint sensors [22, 23].

PMUT performance largely depends on the type of piezoelectric material and device geometry. PZT is the most commonly used material, offering a high transverse piezoelectric coefficient $e_{31,f}$, which enhances coupling coefficient ($k_t^2 \propto e_{31,f}^2/\epsilon_{33}$) and boosts transmit sensitivity ($S_{TX} \propto e_{31,f}$). However, $e_{31,f}$ materials like PZT have lower receive sensitivity ($S_{RX} \propto e_{31,f}/\epsilon_{33}$) compared to AlN due to their high dielectric constant. Sc doping in AlN improves k_t^2 while while maintaining high S_{RX}, making it suitable for low-power applications [24, 25, 26].

Numerous studies have attempted to structurally modify the conventional clamped membrane to enhance key performance metrics, such as displacement sensitivity, transmit sensitivity, linearity, and bandwidth. Wang et al. [27] demonstrated a square PMUT operating at 2.3 MHz, which incorporated three rows of etching holes around the boundary. This design produced a piston-like membrane mode shape, resulting in a 5.3 dB increase in transmitted acoustic pressure and improved directivity. Piston-like motion refers to the near-uniform vertical displacement of the membrane, where the central region is lifted or lowered tangentially from the edges, resulting in improvement in effective acoustic area and transmission efficiency. The same authors also introduced a multi-mode broadband

PMUT, where resonant modes above 1 MHz converged to achieve a wide bandwidth in damped media, utilizing a rectangular membrane with a high length-to-width aspect ratio [28]. Chen et al. [29] utilized V-shaped spring geometries in PMUT designs to confine stress concentrations, enabling the realization of a flattened vibrating diaphragm. This design achieved a 203% increase in displacement sensitivity and a 23 dB enhancement in output sound pressure compared to traditional designs. Simulation and modeling work on a piston diaphragm atop a conventional AlN membrane operating in multi-mode was reported in [30]. This study demonstrated a 2.4 dB increase in far-field Sound Pressure Level (SPL) and a 1.4-fold increase in bandwidth compared to traditional PMUT designs. Ledesma et al. [31] developed a square AlN PMUT with four linear holes at the edge, which doubled the transmit and receive sensitivity compared to a clamped PMUT. Additionally, a Si_3N_4 passivation layer was applied to seal the cavity, enabling operation in liquid at 2.1 MHz. Rozen et al. [32] integrated concentric rings into the PMUT design to amplify overall SPL by channeling the pressure generated from the backside to the front side. This modification led to a 4.4 dB increase in far-field SPL. Another study presented a residual stress-free AlN PMUT with frame-like outer electrodes, operating at 2.2 MHz, which achieved a perfectly flat membrane and eliminated initial buckling. This design resulted in a 450% increase in transmitting sensitivity compared to conventional PMUTs [33]. Akhbari et al. [34] developed an AlN PMUT with a curved diaphragm, featuring a 140 µm diameter and a 1 mm radius of curvature, operating at 2.2 MHz. This design achieved DC displacement sensitivity approximately 50 times greater than that of a similarly sized planar device, although it introduced increased fabrication complexity. A beam–membrane coupled PMUT employing three peripheral beams with central anchoring was reported by Qu et al. [35], where the anchored center caused the outer beam edges to deflect upward and enhance coupling with the membrane; however, no linearity characterization or air-coupled pressure measurements were performed. Xu et al. [36] designed a 215 kHz PMUT diaphragm with six tiltable cantilever actuators to excite a piston mode, which improved the linear vibration range compared to conventional PMUTs, while also enabling mechanical steering of the ultrasonic beam.

Unlike conventional clamped membrane designs optimized for MHz or high-kHz operation, this work presents measurement and analysis of $Sc_{0.3}Al_{0.7}N$ PMUTs operating in the low-frequency range of 45–75 kHz, specifically engineered to achieve piston-like motion. This study introduces a structure with intentional circumferential curvature of the peripheral actuation elements, where the beams or cantilevers are geometrically curved along the boundary of the PMUT membrane. These curved elements act as actuators in conjunction with the membrane, enabling simultaneous excitation of both the central and outer regions to improve linearity and transmit sensitivity. Additionally, a comprehensive linearity analysis is conducted, along with a detailed performance comparison against conventional PMUTs. Given the limited studies on structural modifications for low-frequency PMUTs and the lack of insights into their linearity [36], this work aims to fill that gap and provide a benchmark against state-of-the-art designs. This research expands upon the authors' previous conference work of a cantilever-actuated PMUT [37]. The current study offers comprehensive measurements, modeling, and performance evaluations of three PMUT designs: conventional PMUT (C-PMUT), curved-cantilever PMUT (CC-PMUT), and curved-beam PMUT (CB-PMUT), where the curvature is a mechanical feature of the peripheral support structures used to induce piston-like displacement in the membrane. This work paves the way for more sensitive and linear PMUT devices in this critical application area.

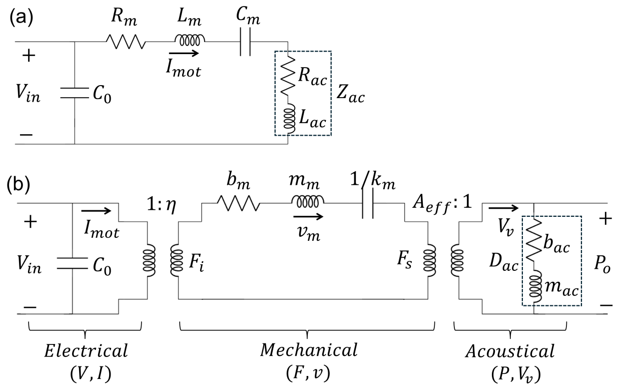

Figure 3: (a) Electrical equivalent model of the transducer. (b) Ultrasound transducer model integrating electrical, mechanical, and acoustical elements.

The following section details the PMUT design, geometric specifications with cross-section, and fabrication process steps. Section 3 provides an in-depth analysis of PMUT characterization, including line profile measurement of the PMUTs and the effect of DC voltage on membrane shape. This section also encompasses mechanical characterization through a Laser Doppler Vibrometer (LDV), focusing on frequency response characteristics, mode shape analysis and electro-mechanical-acoustical modeling. Section 4 investigates the device's linearity through broadband chirp input analysis and explores the impact of increasing AC input voltage levels. The study provides detailed measurements of transmit and receive sensitivities, benchmarking these results against state-of-the-art literature. Additionally, the radiation patterns of PMUTs are measured to calculate the Field of View (FOV) and directivity of PMUTs. Section 5 presents measurement results from long-distance pitch-catch experiments, including receive voltage and signal-to-noise ratio (SNR) calculations, followed by concluding remarks.

2 PMUT design and fabrication

Three distinct types of 30% Sc-doped PMUTs were designed to operate in the frequency range of 45-75 kHz. Fig. 1(a) shows an optical micrograph of the C-PMUT, featuring a clamped membrane with a diam-

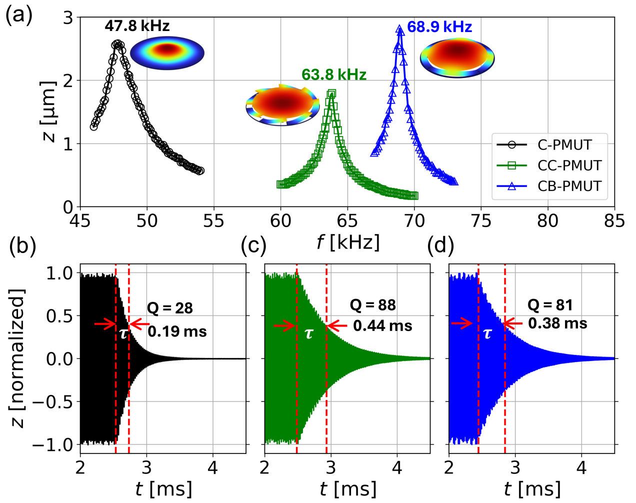

Figure 4: (a) LDV measured frequency response of C-PMUT, CC-PMUT, and CB-PMUT at 2.5 V_{pp}, with simulated mode shapes at resonance. (b) Time-domain mechanical response showing normalized displacement, ring-down decay, and extracted Q factors for (b) C-PMUT, (c) CC-PMUT, and (d) CB-PMUT.

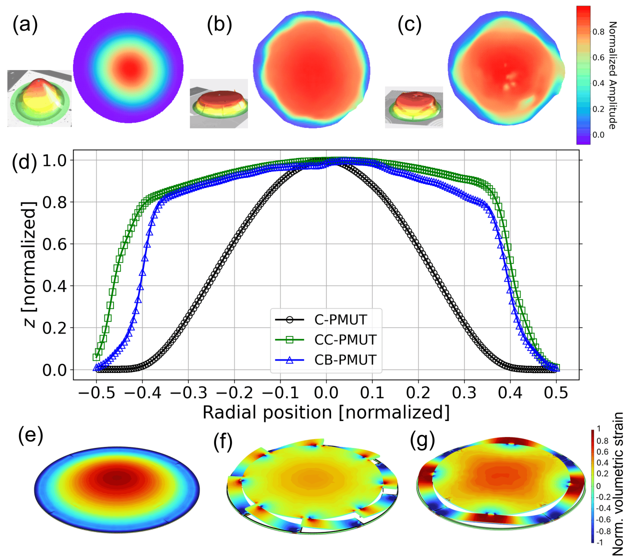

Figure 5: Measured 3D vibrational mode shape at resonance for (a) C-PMUT, (b) CC-PMUT, and (c) CB-PMUT. (d) Line profile showing the variation of normalized vertical displacement with normalized radial position. Normalized volumetric strain showing tensile and compressive regions of stress at resonant modes of (e) C-PMUT (f) CC-PMUT, and (g) CB-PMUT, respectively.

eter of 1800 µm and 70% electrode coverage, designed to operate at approximately 50 kHz. Figs. 1(b) and (c) showcase the configurations of CC-PMUT and CB-PMUT, both designed for operation around 65 kHz, with a diameter of 875 µm. The CC-PMUT incorporates eight curved cantilevers, whereas the CB-PMUT features four curved beams along its edges. The diameters, cantilever and beam widths, as well as the associated coupler widths, are directly labeled in the figure for clarity. In both CC-PMUT and CB-PMUT, the electrodes cover the entire region of the central membrane and edge actuators. Fig. 1(d) illustrates the cross-section of the CB-PMUT along the A-A' cut-line. The device structure, fabricated on a 9 µm thick silicon layer, consists of a released curved beam and a central membrane. The design incorporates a ScAlN piezoelectric layer with a thickness of 1 µm, flanked by upper and lower Molybdenum (Mo) electrodes, each measuring 200 nm in thickness. For clarity, an exploded view of the device, displaying the different layers, is provided in Fig. 1(e). The PMUT is fabricated on Silicon-on-Insulator (SOI) wafer with 9 µm silicon device layer and the process details are available in the supplementary information.

3 PMUT characterization and modeling

This section analyzes the membrane line profile of PMUTs and investigates the impact of varying DC voltage on membrane deformation. The equivalent circuit model is first introduced, followed by mechanical characterization using LDV. The mode shapes are measured using LDV, while FE simulations are utilized to analyze the effective area and stress distribution. Finally, the extracted model parameters are summarized in a tabular format.

3.1 PMUT profile

Previous research has shown that DC bias affects both the polarization and intrinsic stress of the piezoelectric layer, resulting in frequency shifts and changes in bandwidth [38, 39]. To analyze the effect of DC voltage on the membrane profile, a profilometer (SENSOFAR S neoX) was used with DC voltage varying from -60 V to +60 V in 20 V increments. A voltage bias was applied to the top electrode, while the bottom electrode remained grounded. Fig. 2(a), (b), and (c) shows the vertical deflection along the cutline marked in the 2D surface profile for C-PMUT, CC-PMUT, and CB-PMUT, respectively. The ScAlN layer exhibits an average tensile stress of 100-150 MPa fabricated from Lab-in-Fab 8-inch line [40], causing the central membrane to bend downward, while the outer edges of the curved cantilevers and beams rise by approximately 1 µm relative to the surrounding flat surface. The C-PMUT bends downward by 2.5 µm, while the CC-PMUT and CB-PMUT exhibit downward deflections of 3.2 µm and 2 µm, respectively. Applying a negative voltage reduces the downward buckling and attempts to flatten the membrane. The conventional clamped membrane is more sensitive to residual stress and bias changes, showing a DC voltage displacement sensitivity value of 33 nm/V. In contrast, the CB-PMUT displays a sensitivity of 20 nm/V, while the CC-PMUT exhibits the lowest sensitivity of approximately 15 nm/V.

3.2 Equivalent model

The basic electrical equivalent model of the PMUT is represented in Fig. 3(a). An input voltage V_{in} ap-

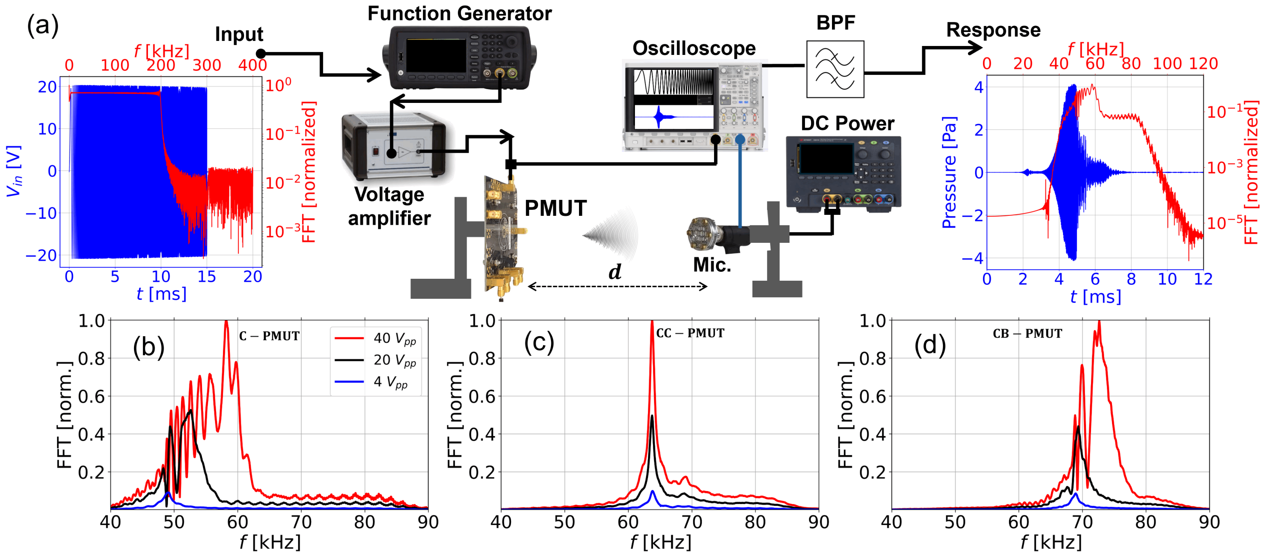

Figure 6: (a) Measurement setup depicting the broadband chirp input applied to the PMUT and the resulting pressure response captured by the microphone. The time-domain waveform and FFT are shown for both input and output signals with a 40 V_{pp} input applied to the C-PMUT. Normalized FFT of the pressure response measured for (b) C-PMUT, (c) CC-PMUT, and (d) CB-PMUT at 4 V_{pp}, 20 V_{pp} and 40 V_{pp} chirp input.

plied across the static capacitor C_0 of the PMUT generates a motional current I_{mot} flowing through the device. R_m represents the motional resistance, which is analogous of membrane damping b_m, the inductance L_m reflects the mass of the membrane m_m, and C_m indicates the capacitance associated with the stiffness k_m of the membrane. The air-medium interface is characterized by Z_{ac}, with its real part, the radiation resistance R_{ac}, representing the power transmitted or received through the air.

A more detailed equivalent model that incorporates the electrical (voltage and current), mechanical (force and velocity), and acoustical (pressure and volume velocity) domains is shown in Fig. 3(b). The transduction factor η quantifies the conversion of input voltage into mechanical force F_i applied to the membrane, resulting in membrane vibrations with velocity v_m. The mechanical parameters of the membrane are linked to η through relationships: $b_m = \eta^2 R_m$, $m_m = \eta^2 L_m$ and $k_m = \eta^2/C_m$. Using the measured displacement amplitude $z(f_0)$ at resonance and equating the spring force $k_m z(f_0)$ with voltage across piezoelectric element QV_{in}, the value of η can be computed using the relation [4]

$$\eta = \frac{QV_{in}C_m}{z(f_0)}. \tag{1}$$

The effective area of the PMUT transforms the membrane velocity into the volume velocity V_v of the air ($V_v = A_{eff}v_m$). It can also be represented as the ratio of force generated on the surface of membrane F_s to the output pressure on surface P_0, given as $A_{eff} = F_s/P_0$. The effective area can be estimated by FE analysis by simulating the PMUTs' frequency response and resonant mode shapes. The effective PMUT area depends on the membrane's spatial displacement distribution, calculated as

$$A_{eff} = \frac{\int_A z\, dA}{z_{max}} \tag{2}$$

where z is the vertical displacement at a point, integrated over the entire membrane area A, and z_{max} is the maximum displacement on the top surface.

The acoustic impedance D_{ac} of the membrane governs the pressure exerted on its front and back surfaces during vibration ($P_0 = V_v D_{ac}$). However, the radiated pressure in the surrounding medium is given by the real part of acoustic impedance as $P_r = V_v\,\mathrm{Re}(D_{ac})$. For clamped membrane, the acoustic impedance can be calculated using the expression [41]

$$D_{ac} = \frac{Z_0}{A_{eff}}\left(1 - \frac{2J_1(2k_w a_{eff})}{2k_w a_{eff}} + j\frac{2K_1(2k_w a_{eff})}{2k_w a_{eff}}\right) \tag{3}$$

where the first order Bessel function is denoted by J_1 and Struve function by K_1. The specific acoustic impedance of air Z_0 is given by the product of its density and velocity ($Z_0 = \rho_{air}c_{air} \approx 412$ Rayl). The wavenumber k_w, depends on the wavelength λ of the propagating wave ($k_w = 2\pi/\lambda$), and the effective radius of the membrane is denoted by a_{eff}. For clamped PMUT, A_{eff} is one-third of the actual area, giving $a_{eff} = a/\sqrt{3}$. The radiation resistance R_{ac} represents the real power transmitted to the air as sound and is calculated using the acoustic impedance with the relation

$$R_{ac} = \mathrm{Re}(D_{ac})\frac{A_{eff}^2}{\eta^2}. \tag{4}$$

Conversely, the reactive component L_{ac} represents the energy temporarily stored due to the air's compressibility, which affects the phase relationship between the membrane's velocity and the pressure generated in the air. The calculation of acoustic impedance is also explained in the supplementary information.

To calculate all the model parameters, the following sequence was followed. First, the impedance-frequency response was measured within the desired frequency range. The total resistance $R = R_m + R_{ac}$, inductance

$L = L_m + L_{ac}$, and the capacitance C_m was determined by fitting the measured data. LDV measurements was used to measure the Q factor, the peak displacement at resonance $z(f_0)$, and membrane velocity v. The transduction factor η was calculated using Eq. 1 and the related mechanical parameters were derived. The effective area A_{eff} was estimated using Eq. 2. R_{ac} and L_{ac} were derived from the real and imaginary parts of the complex acoustic impedance D_{ac}, using Eq. 3 and Eq. 4. The coupling coefficient k_t^2 was calculated using the ratio of motional and static capacitances using $k_t^2 = C_m/(C_m + C_0)$.

3.3 PMUT response

The mechanical response of the PMUTs was characterized using LDV, where a 1 V_{pp} sinusoidal signal was applied with the frequency sweeping around the resonance point. Monitoring the displacement at the center of the membrane revealed the devices' resonant behavior. The Q-factor was calculated from the ring-down response at resonance using the relation $Q \approx \pi f \tau \approx 1/\text{FBW}$, where τ is the decay time, defined as the time it takes for the PMUT response to decrease to $1/e$ of its maximum value and FBW is the fractional bandwidth of the PMUT [42]. The measured Q factor was used in the equivalent model. FE simulations were used to assess the vibration mode shape of the PMUTs at resonance. Fig. 4(a) shows the displacement–frequency response, including the mode shape, and resonance, indicated on the figure. Fig. 4(b), (c), and (d) present the time-domain responses of the C-PMUT, CC-PMUT, and CB-PMUT, respectively, displaying the normalized membrane displacements at resonance, with the corresponding decay time constants and Q-factors highlighted. Both CC-PMUT and CB-PMUT exhibit similar piston-like mode shapes, with the CB-PMUT producing the largest central displacement.

The mode shapes of the PMUTs at resonance were analyzed using LDV under continuous sinusoidal excitation. Fig. 5(a), (b), and (c) show the 3D and top-down views of the normalized displacement profiles at resonance for C-PMUT, CC-PMUT, and CB-PMUT, respectively. Fig. 5(d) illustrates the variation in normalized vertical displacement along the normalized horizontal radial position of the PMUTs. The conventional C-PMUT exhibits a typical Gaussian (tent-like) mode shape, while the CC-PMUT and CB-PMUT display piston-like motion due to the simultaneous actuation of the curved actuator and central membrane, resulting in larger vertical displacement areas. Simulations estimate the effective area to be approximately 35% for the C-PMUT, consistent with the theoretical prediction of one-third [23], and around 65% and 60% for the CC-PMUT and CB-PMUT, respectively. Fig. 5(e), (f), and (g) show the normalized volumetric strain for the C-PMUT, CC-PMUT, and CB-PMUT. In the C-PMUT, about 70% of the membrane diameter is under tensile strain, while the remaining regions experience compressive stress. For CC-PMUT and CB-PMUT, the raised upper half of the cantilevers or beams, along with most of the central membrane area, experience tensile stress, while the lower half of the clamped cantilevers or beams are under compression.

Table 1: PMUT parameters from equivalent model

Property	Parameter	Symbol	Device		
			C-PMUT	CC-PMUT	CB-PMUT
Electrical	Resistance	R_m (kΩ)	47.4	168.2	66.8
	Radiation resistance	R_{ac} (kΩ)	12.4	57.4	29.4
	Inductance	L_m(H)	5.3	48.5	17.7
	Acoustic inductance	L_{ac} (H)	0.2	0.6	0.3
	Capacitance	C_m (pF)	2	0.13	0.3
	Static capacitance	C_0 (pF)	256	86.2	88.5
	Motional current	I_{mot} (µA)	16.7	4.4	10.4
Mechanical	Transduction factor	η (μN/V)	53.7	15.4	21.4
	Damping	b_m (µNs/m)	136.4	39.7	30.5
	Acoustic damping	b_{ac} (µNs/m)	35.8	13.6	13.4
	Mass	m_m (ng)	15.2	11.5	8.1
	Acoustic mass	m_{ac} (ng)	0.433	0.137	0.121
	Stiffness	k_m (N/m)	1412.3	1862.3	1529
	Displacement	z (nm)	1035.2	718.9	1125.7
	Velocity	v (mm/s)	311.6	288.1	486.2
Acoustical	Effective area	A_{eff} (mm^2)	0.848	0.391	0.361
	Impedance	$Re(D_{ac})$ (Rayls/mm^2)	49.7	88.8	102.9
	Mass-density	ρ_{ac} (μg/mm^2)	511	350.4	335.2
	Volume velocity	V_v (mm^3/s)	264.3	121.6	175.4
Other	Frequency	f_0 (kHz)	47.9	63.8	68.7
	Coupling coefficient	k_t^2 (%)	0.98	0.18	0.42
	Q-factor	Q	27.25	87.16	80.72
	Transmit	S_{TX} (Pa/V)	13.14	10	18.05
	Receive	$S_{RX,oc}$ (mV/Pa)	4.25	4.34	6.52
		$S_{RX,sc}$ (nA/Pa)	333.35	150.95	251.43

The values of I_{mot}, z, v and V_v are specified for 1 V input.

Table 1 summarizes the electrical, mechanical, and acoustical parameters of the three PMUTs under test. For the receiving configuration, the acoustic port serves as the input port, while the open-circuit voltage or short-circuit current is determined as the output at the electrical port. The transmit sensitivity S_{TX}, for a 1 V input, along with the open-circuit and short-circuit receive sensitivities S_{RX}, for a 1 Pa input, are presented in the table. The simplified model indicates that the CB-PMUT is anticipated to exhibit higher transmit sensitivity, while the receiving sensitivity of all the PMUTs tested is expected to range between 4 mV/Pa to 7 mV/Pa. The electrical impedance response was measured for all PMUTs using a 100 mV AC signal while varying the DC voltage from -40V to 40V in 5V increments. The results are provided in the supplementary information.

4 Linearity, sensitivity & radiation pattern

This section presents the experimental results on the linearity, sensitivity, and radiation patterns of the PMUTs. Broadband chirp analysis and LDV are employed to evaluate the linearity of the PMUTs. The transmit (TX) sensitivity is assessed in terms of displacement and pressure, while the receive (RX) sensitivity is determined by measuring the pressure and correlating it with the corresponding received voltage. The radiation patterns of each PMUT type are also measured. Finally, the sensitivity results are benchmarked against values documented in prior research.

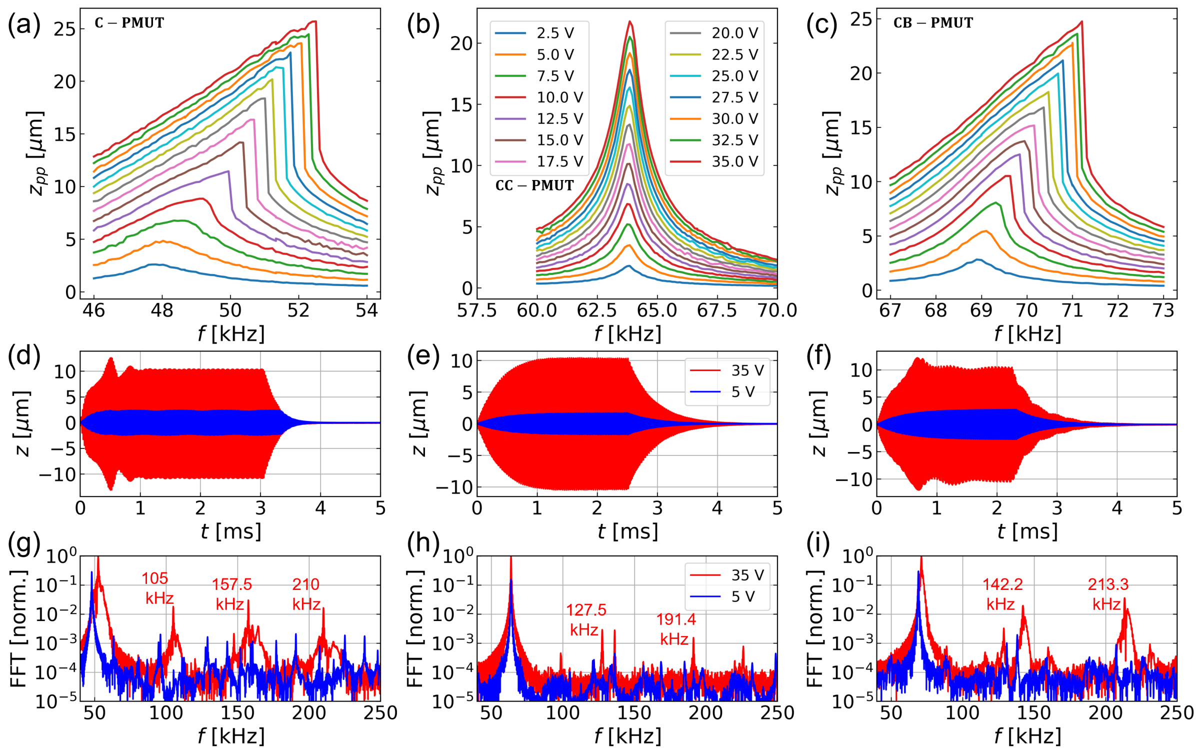

Figure 7: Frequency response illustrating the peak-to-peak displacement z_{pp} measured by LDV for (a) C-PMUT, (b) CC-PMUT, and (c) CB-PMUT. The time-domain displacement signals for 5 V_{pp} and 35 V_{pp} are presented for (d) C-PMUT, (e) CC-PMUT, and (f) CB-PMUT. The corresponding FFT of the displacement signals for 5 V_{pp} and 35 V_{pp} are shown for (g) C-PMUT, (h) CC-PMUT, and (i) CB-PMUT.

4.1 Linearity assessment

Fig. 6 illustrates the measurement setup for evaluating the linearity of the PMUTs. A linear chirp is generated using the arbitrary waveform feature of a function generator (Keysight 33500B), amplified 50 times by a voltage amplifier (Falco Systems WMA-300), and then applied to the transmitting PMUT wirebonded onto a custom Printed Circuit Board (PCB). The frequency of the applied chirp signal linearly increases from an initial value of $f_i = 100$ Hz to a final value of $f_f = 200$ kHz within chirp duration T_{ch} of 15 ms. The input signal follows the equation

$$V_{\text{in}}(t) = \begin{cases} A \sin\left(2\pi \left(\frac{r_{ch}}{2} t^2 + f_i t\right)\right), & \text{for } t \leq 15\,\text{ms} \\ 0, & \text{for } t > 15\,\text{ms} \end{cases} \tag{5}$$

where A is the amplitude and $r_{ch} = (f_f - f_i)/T_{ch}$ denotes the chirp rate. The input peak-to-peak voltage is varied from 2 V to 40 V in 2 V increments to study the effect of increasing AC voltage on the device's response. A microphone (Avisoft-Bioacoustics CM16/CMPA40-5V) positioned at a distance $d \approx 15$ cm from the PMUT records the pressure waveform and converts it to an electrical signal with a sensitivity of 1.4 V/Pa. A DC power supply (Keysight E36313A) provides the microphone with a 5 V bias. The applied and received signals are monitored on an oscilloscope (Keysight DSO-X 4024A). The received signal is bandpass-filtered within the 40–85 kHz range, and its time-domain waveform and Fast Fourier Transform (FFT) are analyzed. Fig. 6 shows a case where a 40 V_{pp}, 200 kHz broadband linear chirp of 15 ms duration is applied as input to the C-PMUT and its time-domain pressure response with FFT is measured. Transmit sensitivity analysis (shown in Fig. 8) employs a similar setup but replaces the chirp signal with a sinusoidal signal swept around the resonance point, measuring the resulting pressure.

Fig. 6(b), (c), and (d) presents the normalized FFT response for C-PMUT, CC-PMUT, and CB-PMUT, respectively, for input voltages of 4 V_{pp}, 20 V_{pp}, and 40 V_{pp}. In the case of C-PMUT, when the input voltage reaches 20 V, the primary frequency peak begins to split due to non-linearity. As the voltage increases further, the resonance frequency shifts higher, indicating a non-linear hardening effect on the membrane. This effect causes vibrational energy to spread across multiple frequency peaks. At 40 V, the resonance frequency has increased by 18% compared to its value at 4 V. The CC-PMUT response demonstrates high linearity, maintaining its resonance at 63.7 kHz despite the increasing voltage. Similarly, the CB-PMUT response, remains predominantly linear up to 20 V and shows an overall 5% increase in resonance frequency.

LDV measurements were carried out by applying a sinusoidal input signal with V_{pp} ranging from 2.5 V to 35 V in 2.5 V increments. The signal frequency swept around the resonance point with 150 input cycles ensured a fully saturated maximum displacement response. The peak-to-peak displacement at the center of the membrane z_{pp} was noted for each input frequency. Pressure measurements followed a similar protocol to determine the peak-to-peak pressure P_{pp} generated by

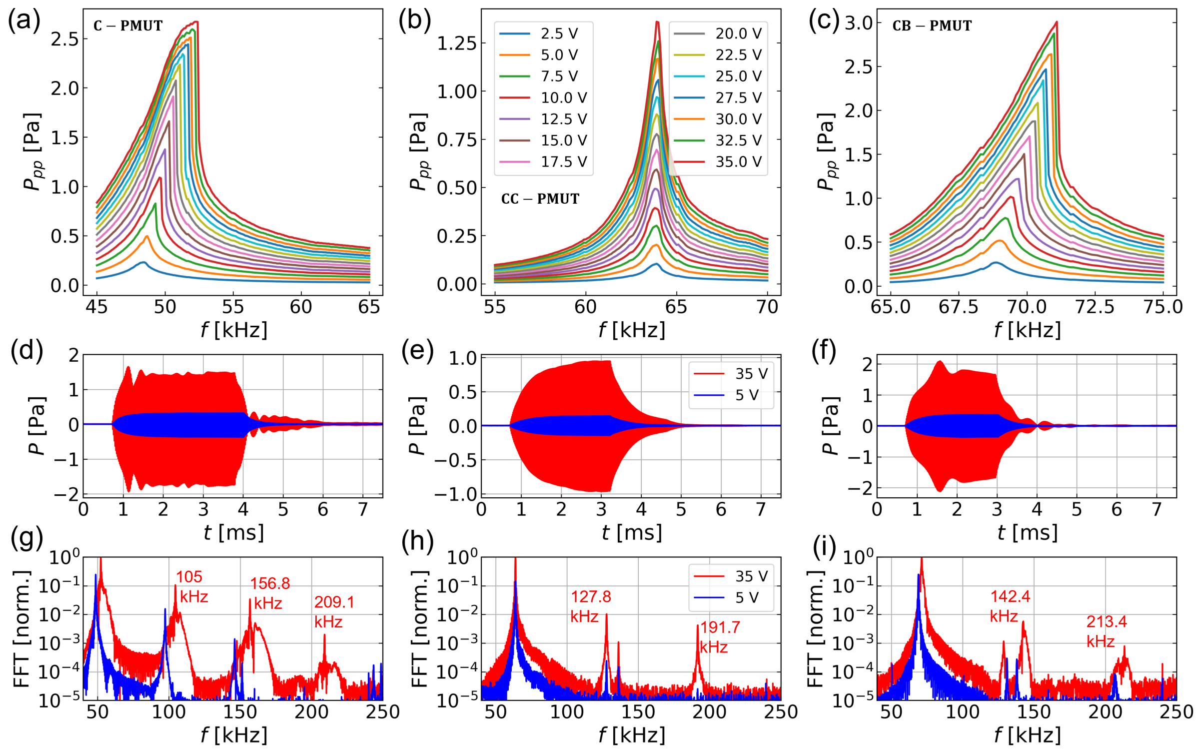

Figure 8: Frequency response illustrating the peak-to-peak pressure P_{pp} measured by microphone at 25 cm distance for (a) C-PMUT, (b) CC-PMUT, and (c) CB-PMUT. The time-domain pressure signals for 5 V_{pp} and 35 V_{pp} are presented for (d) C-PMUT, (e) CC-PMUT, and (f) CB-PMUT. The corresponding normalized FFT of the pressure signals for 5 V_{pp} and 35 V_{pp} are shown for (g) C-PMUT, (h) CC-PMUT, and (i) CB-PMUT.

the PMUTs. A microphone, positioned 25 cm from the PMUTs, recorded the pressure as V_{pp} increased incrementally.

Fig. 7(a), (b), and (c) display the displacement responses near resonance for C-PMUT, CC-PMUT, and CB-PMUT, respectively. The displacement at the center of the membrane increases with the input voltage, reaching about 25 µm at 35 V for C-PMUT and CB-PMUT. CC-PMUT maintains linear characteristics while C-PMUT and CB-PMUT show non-linear behavior with increasing resonance frequency at higher voltages. Fig. 7(d), (e), and (f) present time-domain displacement signals for 5 V and 35 V cases, with corresponding FFT responses in Fig. 7(g), (h), and (i). At 35 V, C-PMUT and CB-PMUT exhibit signal distortion with distinct harmonic frequency peaks. C-PMUT generates harmonics at 105 kHz, 157.5 kHz, and 210 kHz, while CB-PMUT produces harmonics at 142.2 kHz and 213.3 kHz. In contrast, CC-PMUT shows a stable displacement signal with minimal frequency variations across voltage levels.

Pressure measurements yielded results consistent with displacement data. Fig. 8(a), (b), and (c) illustrate the pressure response with frequency near resonance for C-PMUT, CB-PMUT, and CC-PMUT, respectively. At 10 V input and 25 cm distance, C-PMUT is able to generate 1.1 Pa (94.8 dB SPL) and CB-PMUT produced a comparative 1 Pa (94 dB SPL), both exhibiting non-linear behavior with increasing voltage. CC-PMUT generates lower pressure (0.39 Pa) in comparison but maintains linearity. Fig. 8(d), (e), and (f) display time-domain pressure signals for 5 V and 35 V cases, with corresponding FFT responses in Fig. 8(g), (h), and (i). The pressure measurements corroborated the displacement results, demonstrating that PMUTs produced harmonics at similar frequency locations under increased input voltage.

Duffing non-linearity refers to a type of cubic mechanical non-linearity observed in resonators, where the displacement response does not increase linearly with increasing excitation amplitude. It can lead to amplitude-dependent resonance shifts (hardening or softening) and distortion, often modeled by a nonlinear spring term in the governing equation of motion. The equation of motion incorporating the third-order stiffness term k_3 is expressed as [43]

$$\ddot{z} + 2(\zeta_1 + \zeta_3 z^2)\omega_0 \dot{z} + \omega_0^2 z + \frac{k_3}{m_{eff}} z^3 = \frac{F}{m_{eff}}, \quad (6)$$

where F is the external force applied, $\omega_0 = 2\pi f_0$ is the angular frequency, and m_{eff} represents the effective mass of the resonator. The terms ζ_1 and ζ_3 represent the linear and third-order damping coefficients, respectively, shaping vibration dynamics at low and high amplitudes that significantly influence the Q-factor of the device. The third-order stiffness term k_3 leads to an amplitude-induced frequency variation. At a steady state, the frequency can be related to the unperturbed frequency through the Duffing coefficient as

$$f = f_0 + \frac{3k_3 z^2}{32\pi^2 f_0 m_{eff}}. \quad (7)$$

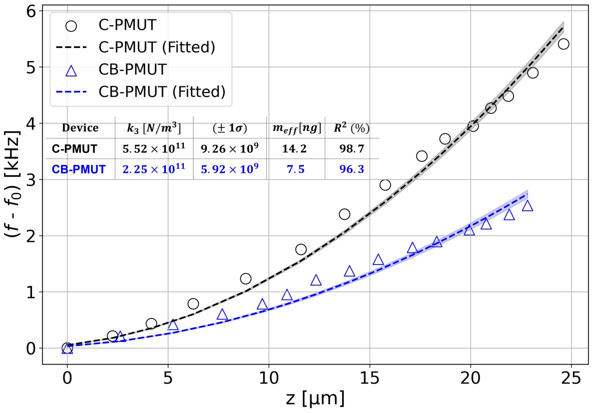

Figure 9: Variation of relative frequency shift with measured displacement for C-PMUT and CB-PMUT, illustrating the fitted value of the conservative Duffing coefficient k_3. The shaded region around the fitted curve represents the $\pm 1\sigma$ uncertainty in k_3. The coefficient of determination (R^2) indicates the goodness of fit and validity of the model.

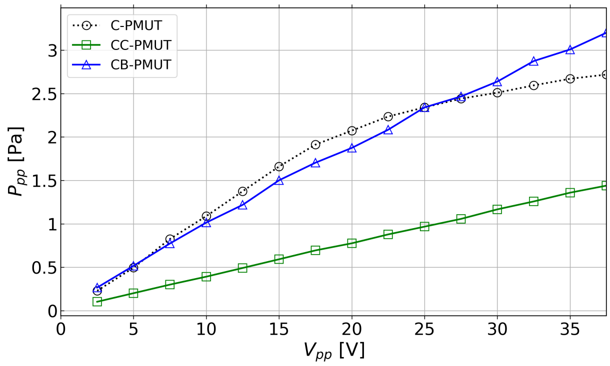

Figure 10: (a) Variation of peak-to-peak displacement z_{pp} and (b) peak-to-peak pressure P_{pp} with peak-to-peak input voltage V_{pp} for C-PMUT, CC-PMUT, and CB-PMUT.

The procedure to fit and extract the non-linear spring stiffness is shown in the supplementary information. The CC-PMUT demonstrates high linearity, maintaining a frequency of 63.8 kHz. Both the C-PMUT and CB-PMUT exhibit non-linearity, with their relative frequency change $f - f_0$ plotted against the measured displacement in Fig. 9, obtained through LDV. The fitted curves using Eq. 7 indicates that the frequency shift is more pronounced for the C-PMUT, as its k_3 value is 2.5 times greater than that of the CB-PMUT.

4.2 Transmit and receive sensitivity

The displacement and pressure sensitivities are determined from the slopes of their respective variations with the driving voltage. Within the range of 10 V, the CB-PMUT exhibits the highest displacement sensitivity, with a maximum of 1025 nm/V, followed by the C-PMUT at 825 nm/V and the CC-PMUT at 610 nm/V. Regarding pressure sensitivity, the C-PMUT achieves 110 mPa/V, while the CC-PMUT produces 40 mPa/V, and the CB-PMUT delivers 102 mPa/V. As shown in Fig. 10, despite being approximately four times smaller in area, the CB-PMUT generates pressure levels comparable to those of the C-PMUT. The pressure response of the C-PMUT begins to saturate beyond 15 V due to increasing non-linearity, whereas the CB-PMUT continues to generate higher pressure. This behavior can be attributed to the reduction in transmission efficiency of the C-PMUT at higher driving voltages, resulting from its pronounced non-linearity compared to the CB-PMUT. Additionally, the CB-PMUT achieves higher membrane vibration velocity, further contributing to its superior performance. The receive sensitivity of the PMUTs was determined using a setup similar to the one depicted in Fig. 6. A 10 V peak-to-peak signal, with its frequency swept around the resonance, was applied to the transmitting PMUT. The resulting pressure-frequency response was measured us-

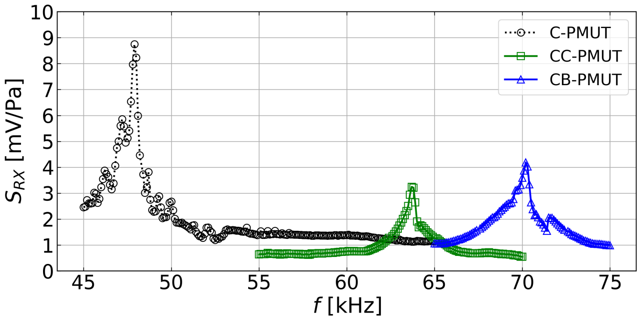

Figure 11: Measured receive sensitivity of C-PMUT, CC-PMUT and CB-PMUT.

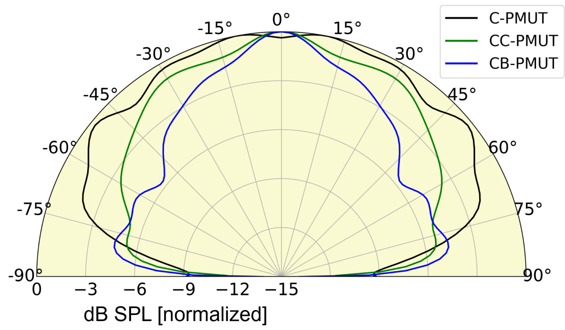

Figure 12: Measured radiation patterns of C-PMUT, CC-PMUT, and CB-PMUT.

ing a microphone positioned at a distance of 25 cm. After completing the pressure measurements, the microphone was replaced with a similar PMUT to record the RX voltage. The RX voltage-frequency response was normalized against the measured pressure response to calculate the RX sensitivity, as illustrated in Fig. 11. Among the tested designs, the C-PMUT demonstrated the highest receive sensitivity at 8.7 mV/Pa, while the CC-PMUT and CB-PMUT exhibited sensitivities of 3.3 mV/Pa and 4.2 mV/Pa, respectively. The C-PMUT features an electrode confined to the central 70% of the membrane, resulting in a higher RX voltage in response to stress. In contrast, the CC-PMUT and CB-PMUT have a single electrode that spans the entire membrane, including the central region and edge actuators, which leads to a reduction in the net charge generated due to stress.

4.3 Radiation Pattern

The far-field pressure at any radial distance r from a vibrating baffled piston is given by the relationship [41]

$$P(r,\theta) = \frac{P_0 R_0}{r} e^{-\alpha r} D(\theta) \tag{8}$$

where P_0 represents the pressure at the surface of the membrane and R_0 is the Rayleigh distance, defined as the ratio of the effective area to the wavelength ($R_0 = A_{eff}/\lambda = k a_{eff}^2/2$). The attenuation of the acoustic wave in a given medium, typically expressed in dB/cm, is represented by α. The factor $D(\theta) = 48 J_3 \left(k a_{eff} \sin\theta\right) / \left(k a_{eff} \sin\theta\right)^3$ describes the directivity of the vibrating element at any angle θ from the on-axis position with J_3 representing Bessel function of the third order. The designed PMUTs, with $k a_{eff} < 0.5$, suggest an omnidirectional radiation pattern. To measure the radiation pattern, a 5 V peak-to-peak sinusoidal signal is applied to the PMUT at its resonance frequency. The generated pressure is recorded by a microphone placed 15 cm away. The microphone remains stationary while the PMUT is rotated in 5-degree increments from its on-axis position, and the peak-to-peak pressure is recorded at each angle. The pressure is then converted to SPL and normalized for comparison. C-PMUT, CC-PMUT, and CB-PMUT yield a 6 dB field of view (FOV) of 161.6°, 164.8°, and 171°, respectively, with fluctuations primarily caused by wave diffraction at the edges of the PCB.

4.4 Comparison with state-of-the-art

The TX and RX sensitivities of the designed PMUT are compared with other state-of-the-art PMUTs specifically designed to operate below 200 kHz. To ensure a fair comparison, the transmission sensitivity was normalized with respect to voltage and active area. Additionally, the on-axis pressure measurement values were transformed using Eq. 8 to a standardized distance of 30 cm for all cases. For this transformation, the attenuation coefficient α was estimated using the relation: $\alpha_{dB/cm} = 10^{-12} f^2 + 2 \times 10^{-7} f + 0.0035$, where f is the frequency of operation in Hz. This equation accounts for acoustic attenuation in air over a frequency

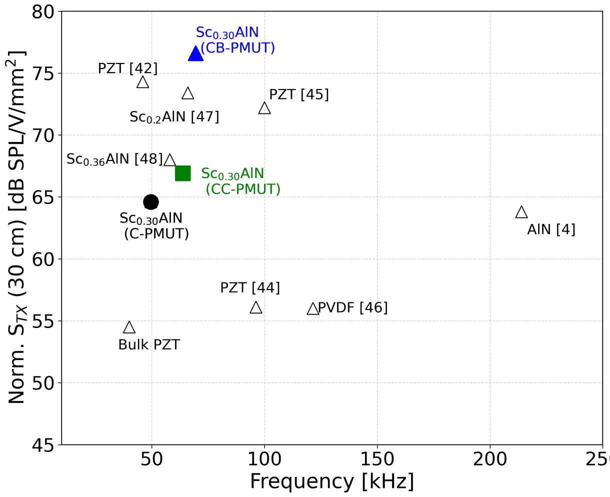

Figure 13: Comparison of normalized transmit sensitivity at a 30 cm distance as a function of frequency for the current work and various reported results.

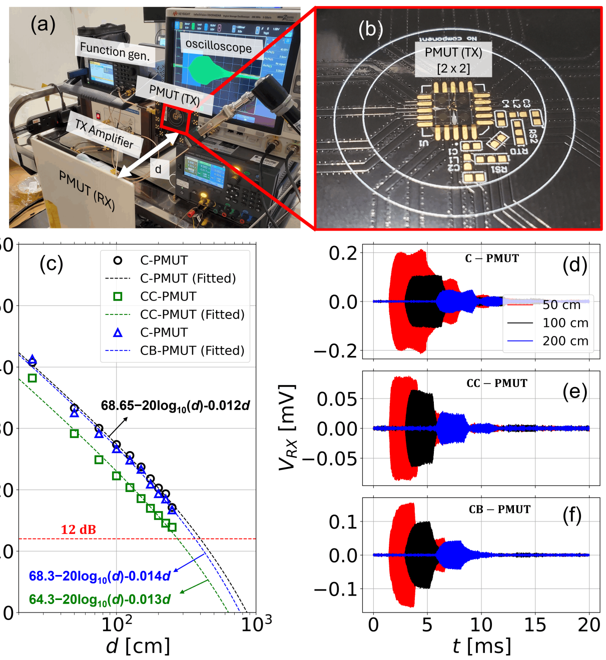

Figure 14: (a) Measurement setup for pitch-catch experiment. (b) PCB with a wire-bonded 2×2 C-PMUT array. (c) Variation of measured signal-to-noise (SNR) ratio with distance for C-PMUT, CB-PMUT and CC-PMUT along with fitted data. Received voltage signal at 50 cm, 100 cm, and 200 cm distance for (d) C-PMUT, (e) CC-PMUT, and (f) CB-PMUT respectively.

Table 2: State-of-the-Art Performance Comparison of Air-Coupled PMUTs

Ref.	Piezoelectric material		Config.	Area	f_0	SPL, distance & voltage			Normalized S_{TX} (30 cm)		S_{RX}
	Type	Thickness μm		mm^2	kHz	dB	cm	V_{pp}	mPa/V/mm^2	dBSPL/V/mm^2	mV/Pa
MA404S commercial	Bulk PZT	--	Array	78.5	40	120	30	24	10.6	54.5	7.1
[44]	PZT	6	Array (37 elements)	4	96.2	117	1.2	10	12.7	56.1	--
[45]	PZT	8	Single	0.61	100	103	3.5	6	81.3	72.2	--
[42]	PZT (single-crystal)	2	Array (2x2)	4.9	46	109.4	26	10	103.7	74.3	1.9
[46]	PVDF	0.5	Single	0.5	121.5	100.8	1	10	12.7	56	--
[4]	AlN	1	Single	0.125	214	84	0.5	1	31	63.8	--
[47]	$Sc_{0.2}AlN$	1.2	Array (14 elements)	11	66	118	20	10	94	73.4	5.7
[48]	$Sc_{0.36}AlN$	1	Array (2x2)	2.26	58	105	10	10	50.3	68	1
This work	$Sc_{0.3}AlN$	1	Single C-PMUT	2.54	49.6	94.4	25	10	33.9	64.6	8.7
			Single CC-PMUT	0.6	63.8	84.2			44.4	66.9	3.3
			Single CB-PMUT	0.6	69.4	93.8			135.6	76.6	4.2

Table 3: Comparison of PMUT Linearity

Ref.	Mat.	Dia. [μm]	Thickness [μm]	f_0 [kHz]	$\Delta f/V_{pp}$ [kHz/V]
[49]	PZT	880	8	61.3	1.26
[50]	ZnO	500	7.1	84	2.1
[42]	PZT	1250	8.7	40	0.4
[51]	AlN	715	8.4	127.5	0.7
[36]	ScAlN	500	8	215	Negligible change up to 6 V_{pp}
C-PMUT	$Sc_{0.3}AlN$	1800	10.6	49.6	0.16
CC-PMUT		875		63.8	Negligible change up to 40 V_{pp}
CB-PMUT		875		69.4	0.08

range of 25 kHz to 300 kHz at 50% relative humidity [52]. By applying these normalization and transformations, a more accurate and meaningful comparison of PMUT performance in dB SPL/V/mm^2 across different designs and operating conditions was made. The current work is compared with commercial bulk transducer, thin-film PZT devices [44, 45], single-crystal PZT [42], polyvinylidene fluoride (PVDF) [46], AlN PMUT [4], and Sc-doped AlN PMUT devices with varying ScAlN concentrations, such as 20% [47] and 36% [48]. Table 2 provides a detailed comparison. The CB-PMUT achieves a normalized sensitivity of 135.6 mPa/V/mm^2, approximately four times higher than that of the C-PMUT. However, the C-PMUT demonstrates the highest RX sensitivity. The normalized sensitivity is also shown in the comparative frequency map in Fig. 13. Among PMUTs operating under 200 kHz, the CB-PMUT demonstrates the highest normalized sensitivity, outperforming PZT and other ScAlN-based devices.

A direct comparison of PMUT non-linearity across the literature is challenging due to differences in operating frequency, device geometry, and the absence of standardized quantification methods. Table 3 summarizes key reports on the non-linear behavior of PMUTs operating below 200 kHz, where the frequency shift per peak-to-peak input voltage ($\Delta f/V_{pp}$) was estimated from published data. Notably, the CC-PMUT and the tiltable-cantilever plate design reported in [36] exhibit minimal resonance drift with increasing drive voltage, while the CB-PMUT also demonstrates high linearity relative to existing designs.

5 Long distance pitch-catch measurement

A pitch-catch experiment was conducted for each PMUT configuration to measure acoustic transmission over a distance of up to 2.5 m. The experimental setup, as depicted in Fig. 14(a), was employed for this purpose. For signal transmission, a 2×2 array configuration (Fig. 14(b)) was driven by a 10 V_{pp} input signal. A single PMUT receiver, mounted on a fixed board, was used to detect signals at varying distances. The received signal was processed through a bandpass filter with a frequency range of 40 kHz to 85 kHz, exhibiting an average noise level of 9.5 µV peak-to-peak. The signal-to-noise ratio (SNR) was calculated using the formula 20 $\log_{10}(V_{RX}/V_n)$, where V_{RX} and V_n represent the peak-to-peak received signal and noise voltage, respectively. The Signal-to-Noise (SNR) values were computed for each distance and plotted, as shown in Fig. 14(c). Data fitting was performed using a model incorporating an attenuation coefficient α ranging from 0.012 dB/cm to 0.014 dB/cm. With a 12 dB SNR threshold, detection ranges of 4 m, 2.7 m, and 3.8 m were achieved for C-PMUT, CC-PMUT, and CB-PMUT, respectively, without using amplifier at the receiver end. The time-domain received voltage signals at distances of 50 cm, 100 cm, and 200 cm are illustrated in Fig. 14(d), (e), and (f) for C-PMUT, CC-PMUT, and CB-PMUT, respectively.

6 Conclusion

This work presents the measurement and analysis of two novel PMUTs that feature curved-cantilever and curved-beam structures designed at the membrane edges to induce piston-like vibrations. The effective area percentage of these devices is approximately doubled compared to conventional PMUTs. The CC-PMUT demonstrates superior linearity with negligible resonance shifts under varying DC or AC voltages, making it ideal for pitch-catch based frequency-sensitive applications such as ultrasound wake-up. In contrast, the CB-PMUT sacrifices some linearity but achieves an enhanced normalized transmit sensitivity of 135.6 mPa/V/mm^2, outperforming both the CC-PMUT and C-PMUT by approximately 3 and 4 times, respectively. The enhanced transmit sensitivity makes the CB-PMUT well-suited for long-range acoustic transmission applications, particularly in dense PMUT arrays and ultrasonic wake-up systems. Future efforts to further improve receive sensitivity could focus on tailoring the electrode layout to selectively cover only the tensile or compressive regions, or by implementing differential drive schemes to mitigate charge cancellation and enhance response. Additionally, the influence of environmental factors such as temperature and humidity on device performance can be investigated to evaluate suitability for real-world deployment.

Acknowledgment

This research is supported by A*STAR under its Industry Alignment Fund – Industry Collaboration Projects (IAF-ICP), with Grant No. I2301E0027, Project Title: Piezo Specialty Lab-in-Fab 2.0 (LiF 2.0).

References

[1] I. Ladabaum, B. Khuri-Yakub, D. Spoliansky, and M. Haller, "Micromachined ultrasonic transducers (muts)," in *1995 IEEE Ultrasonics Symposium. Proceedings. An International Symposium*, vol. 1, 1995, pp. 501–504.

[2] X. Jin, I. Ladabaum, and B. Khuri-Yakub, "The microfabrication of capacitive ultrasonic transducers," *Journal of Microelectromechanical Systems*, vol. 7, no. 3, pp. 295–302, 1998.

[3] P. Muralt, N. Ledermann, J. Paborowski, A. Barzegar, S. Gentil, B. Belgacem, S. Petitgrand, A. Bosseboeuf, and N. Setter, "Piezoelectric micromachined ultrasonic transducers based on pzt thin films," *IEEE Transactions on Ultrasonics, Ferroelectrics, and Frequency Control*, vol. 52, no. 12, pp. 2276–2288, 2005.

[4] R. J. Przybyla, S. E. Shelton, A. Guedes, I. I. Izyumin, M. H. Kline, D. A. Horsley, and B. E. Boser, "In-air rangefinding with an aln piezoelectric micromachined ultrasound transducer," *IEEE Sensors Journal*, vol. 11, no. 11, pp. 2690–2697, 2011.

[5] K. Roy, J. E.-Y. Lee, and C. Lee, "Thin-film pmuts: A review of over 40 years of research," *Microsystems & Nanoengineering*, vol. 9, no. 1, p. 95, 2023.

[6] E. Ledesma, A. Uranga, F. Torres, and N. Barniol, "Fully integrated pitch-matched alscn pmut-on-cmos array for high- resolution ultrasound images," *IEEE Sensors Journal*, vol. 24, no. 10, pp. 15 954–15 966, 2024.

[7] X. Chen, J. Xu, H. Chen, H. Ding, and J. Xie, "High-accuracy ultrasonic rangefinders via pmuts arrays using multi-frequency continuous waves," *Journal of Microelectromechanical Systems*, vol. 28, no. 4, pp. 634–642, 2019.

[8] P. Gijsenbergh, A. Halbach, Y. Jeong, G. B. Torri, M. Billen, L. Demi, C.-H. Huang, D. Cheyns, X. Rottenberg, and V. Rochus, "Characterization of polymer-based piezoelectric micromachined ultrasound transducers for short-range gesture recognition applications," *Journal of Micromechanics and Microengineering*, vol. 29, no. 7, p. 074001, may 2019.

[9] Y. Lu, A. Heidari, and D. A. Horsley, "A high fill-factor annular array of high frequency piezoelectric micromachined ultrasonic transducers," *Journal of Microelectromechanical Systems*, vol. 24, no. 4, pp. 904–913, 2015.

[10] P. Zhang, G. Fitzpatrick, T. Harrison, W. A. Moussa, and R. J. Zemp, "Double-soi wafer-bonded cmuts with improved electrical safety and minimal roughness of dielectric and electrode surfaces," *Journal of Microelectromechanical Systems*, vol. 21, no. 3, pp. 668–680, 2012.

[11] Y. Yu, S. H. Pun, P. U. Mak, C.-H. Cheng, J. Wang, P.-I. Mak, and M. I. Vai, "Design of a collapse-mode cmut with an embossed membrane for improving output pressure," *IEEE Transactions on Ultrasonics, Ferroelectrics, and Frequency Control*, vol. 63, no. 6, pp. 854–863, 2016.

[12] O. Rozen, S. T. Block, X. Mo, W. Bland, P. Hurst, J. M. Tsai, M. Daneman, R. Amirtharajah, and D. A. Horsley, "Monolithic mems-cmos ultrasonic rangefinder based on dual-electrode pmuts," in *2016 IEEE 29th International Conference on Micro Electro Mechanical Systems (MEMS)*, 2016, pp. 115–118.

[13] S. Sadeghpour, S. V. Joshi, C. Wang, and M. Kraft, "Novel phased array piezoelectric micromachined ultrasound transducers (pmuts) for medical imaging," *IEEE Open Journal of Ultrasonics, Ferroelectrics, and Frequency Control*, vol. 2, pp. 194–202, 2022.

[14] I. Zamora, E. Ledesma, A. Uranga, and N. Barniol, "Monolithic single pmut-on-cmos ultrasound system with +17 db snr for imaging applications," *IEEE Access*, vol. 8, pp. 142 785–142 794, 2020.

[15] F. L. Degertekin, "How ultrasound became ultra small," *IEEE Spectrum*, vol. 61, no. 4, pp. 38–43, 2024.

[16] D. E. Dausch, K. H. Gilchrist, J. B. Carlson, S. D. Hall, J. B. Castellucci, and O. T. von Ramm, "In vivo real-time 3-d intracardiac echo using pmut arrays," *IEEE Transactions on Ultrasonics, Ferroelectrics, and Frequency Control*, vol. 61, no. 10, pp. 1754–1764, 2014.

[17] T. Carter, S. A. Seah, B. Long, B. Drinkwater, and S. Subramanian, "Ultrahaptics: multi-point mid-air haptic feedback for touch surfaces," in *Proceedings of the 26th annual ACM symposium on User interface software and technology*, 2013, pp. 505–514.

[18] M. Gao, Z. Tong, Z. Wu, and L. Lou, "An ultrasonic target detection system based on piezoelectric micromachined ultrasonic transducers," *Micromachines*, vol. 14, no. 3, 2023.

[19] Z. Tong, H. Hu, Z. Wu, S. Xie, G. Chen, S. Zhang, L. Lou, and H. Liu, "An ultrasonic proximity sensing skin for robot safety control by using piezoelectric micromachined ultrasonic transducers (pmuts)," *IEEE Sensors Journal*, vol. 22, no. 18, pp. 17 351–17 361, 2022.

[20] F. Pop, S. D. Calisgan, B. Herrera, A. Risso, S. Kang, V. Rajaram, Z. Qian, and M. Rinaldi, "Zero-power ultrasonic wakeup receiver based on mems switches for

implantable medical devices," *IEEE Transactions on Electron Devices*, vol. 69, no. 3, pp. 1327–1332, 2022.

[21] S. Trivedi, D. J. Goh, W. Chen, W. D. Toh, J. Zhang, S. Ghosh, D. Giusti, A. Leotti, H. C. Chan, G. Koppisetti, Y. Zhang, Y. Gao, J. E.-Y. Lee, and Y. Koh, "Long-range ultrasound wake-up receiver using pzt-scaln hybrid pmut link with exponential horn," in *2024 IEEE 37th International Conference on Micro Electro Mechanical Systems (MEMS)*, 2024, pp. 501–504.

[22] X. Jiang, H.-Y. Tang, Y. Lu, E. J. Ng, J. M. Tsai, B. E. Boser, and D. A. Horsley, "Ultrasonic fingerprint sensor with transmit beamforming based on a pmut array bonded to cmos circuitry," *IEEE transactions on ultrasonics, ferroelectrics, and frequency control*, vol. 64, no. 9, pp. 1401–1408, 2017.

[23] X. Jiang, Y. Lu, H.-Y. Tang, J. M. Tsai, E. J. Ng, M. J. Daneman, B. E. Boser, and D. A. Horsley, "Monolithic ultrasound fingerprint sensor," *Microsystems & nanoengineering*, vol. 3, no. 1, pp. 1–8, 2017.

[24] Y. Lu, H.-Y. Tang, S. Fung, B. E. Boser, and D. A. Horsley, "Pulse-echo ultrasound imaging using an aln piezoelectric micromachined ultrasonic transducer array with transmit beam-forming," *Journal of Microelectromechanical Systems*, vol. 25, no. 1, pp. 179–187, 2016.

[25] S. T. Haider, M. A. Shah, D.-G. Lee, and S. Hur, "A review of the recent applications of aluminum nitride-based piezoelectric devices," *IEEE Access*, vol. 11, pp. 58 779–58 795, 2023.

[26] C. B. Karuthedath, A. T. Sebastian, P. Helistö, T. Sillanpää, and A. Kärkkäinen, "Development of scaln pmuts for medical applications," *Journal of Microelectromechanical Systems*, vol. 32, no. 5, pp. 505–512, 2023.

[27] T. Wang, R. Sawada, and C. Lee, "A piezoelectric micromachined ultrasonic transducer using piston-like membrane motion," *IEEE Electron Device Letters*, vol. 36, no. 9, pp. 957–959, 2015.

[28] T. Wang, T. Kobayashi, and C. Lee, "Micromachined piezoelectric ultrasonic transducer with ultra-wide frequency bandwidth," *Applied Physics Letters*, vol. 106, no. 1, p. 013501, 01 2015.

[29] X. Chen, D. Chen, X. Liu, D. Yang, J. Pang, and J. Xie, "Transmitting sensitivity enhancement of piezoelectric micromachined ultrasonic transducers via residual stress localization by stiffness modification," *IEEE Electron Device Letters*, vol. 40, no. 5, pp. 796–799, 2019.

[30] L. Wang, W. Zhu, Z. Wu, W. Liu, and C. Sun, "A novel coupled piezoelectric micromachined ultrasonic transducer based on piston mode," *IEEE Transactions on Ultrasonics, Ferroelectrics, and Frequency Control*, vol. 68, no. 11, pp. 3396–3405, 2021.

[31] E. Ledesma, I. Zamora, A. Uranga, and N. Barniol, "Tent-plate aln pmut with a piston-like shape under liquid operation," *IEEE Sensors Journal*, vol. 20, no. 19, pp. 11 128–11 137, 2020.

[32] O. Rozen, S. T. Block, S. E. Shelton, and D. A. Horsley, "Piezoelectric micromachined ultrasonic transducer with increased output pressure via concentric venting rings," in *2015 Transducers - 2015 18th International Conference on Solid-State Sensors, Actuators and Microsystems (TRANSDUCERS)*, 2015, pp. 670–673.

[33] T. Wang and C. Lee, "Zero-bending piezoelectric micromachined ultrasonic transducer (pmut) with enhanced transmitting performance," *Journal of Microelectromechanical Systems*, vol. 24, no. 6, pp. 2083–2091, 2015.

[34] S. Akhbari, F. Sammoura, S. Shelton, C. Yang, D. Horsley, and L. Lin, "Highly responsive curved aluminum nitride pmut," in *2014 IEEE 27th International Conference on Micro Electro Mechanical Systems (MEMS)*, 2014, pp. 124–127.

[35] M. Qu, X. Chen, K. Zhu, X. Guo, and J. Xie, "Beam-membrane coupled piezoelectric micromachined ultrasonic transducers with enhanced transmitting sensitivity," *Micromachines*, vol. 13, no. 3, 2022.

[36] T. Xu, J. Abbaszadeh, C. Bourquard, A. Darie, and M. Moridi, "Tiltable cantilever-plate based piezoelectric micromachined ultrasonic transducers (pmut) with large linear vibration range and high output power," in *2023 22nd International Conference on Solid-State Sensors, Actuators and Microsystems (Transducers)*, 2023, pp. 132–135.

[37] S. Trivedi, D. J. Goh, P. C. Prakasha Chigahalli Ramegowda, D. S. Choong, J. Liu, D. S. Chen, Y. S. Teo, S. Merugu, H. Yan, Q. X. Zhang, Y. Koh, A. Leotti, R. Shankar, N. G. Zakiyyan, A. Das, and C. Lazzari, "Curved cantilever actuated scaln pmut for enhanced linearity and transmit sensitivity," in *2024 IEEE International Ultrasonics, Ferroelectrics, and Frequency Control Joint Symposium (UFFC-JS)*, 2024, in Press.

[38] Y. Kusano, Q. Wang, R. Q. Rudy, R. G. Polcawich, and D. A. Horsley, "Wideband air-coupled pzt piezoelectric micromachined ultrasonic transducer through dc bias tuning," in *2017 IEEE 30th International Conference on Micro Electro Mechanical Systems (MEMS)*, 2017, pp. 1204–1207.

[39] Y. Gao, L. Zhao, C. Yang, and Y. Lu, "Ultra-wide range frequency tuning of piezoelectric micromachined ultrasonic transducers via dc bias voltage," in *2024 IEEE 37th International Conference on Micro Electro Mechanical Systems (MEMS)*, 2024, pp. 935–938.

[40] J. Liu, G. D. Jian, D. Ssu-Han Chen, D. C. Sze Wai, T. Shyam, P. C. Ramegowda, M. Srinivas, L. Huamao, Z. Q. Xin, P. Chang Hyun Kee, A. Das, A. Sciarrone, A. Leotti, D. Giusti, J. E.-Y. Lee, and Y. Koh, "Towards unparallelled cmos-compatible air-coupled pmut performance with 30analysis of residual stress effects," in *2024 IEEE Ultrasonics, Ferroelectrics, and Frequency Control Joint Symposium (UFFC-JS)*, 2024, pp. 1–4.

[41] D. Blackstock, *Fundamentals of Physical Acoustics.* Wiley-Interscience, 2000.

[42] G.-L. Luo, Y. Kusano, and D. A. Horsley, "Airborne piezoelectric micromachined ultrasonic transducers for long-range detection," *Journal of Microelectromechanical Systems*, vol. 30, no. 1, pp. 81–89, 2021.

[43] T. Kaisar, J. Lee, D. Li, S. W. Shaw, and P. X.-L. Feng, "Nonlinear stiffness and nonlinear damping in atomically thin mos_2 nanomechanical resonators," *Nano Letters*, vol. 22, no. 24, pp. 9831–9838, 2022.

[44] Z. Wang, W. Zhu, J. Mia, H. Zhu, C. Chao, and O. K. Tan, "Micromachined thick film piezoelectric ultrasonic transducer array," in *The 13th International*

Conference on Solid-State Sensors, Actuators and Microsystems, 2005. Digest of Technical Papers. TRANSDUCERS '05., vol. 1, 2005, pp. 883–886 Vol. 1.

[45] G. Massimino, L. D'Alessandro, F. Procopio, R. Ardito, M. Ferrera, and A. Corigliano, "Air-coupled pmut at 100 khz with pzt active layer and residual stresses: Multiphysics model and experimental validation," in *2017 18th International Conference on Thermal, Mechanical and Multi-Physics Simulation and Experiments in Microelectronics and Microsystems (EuroSimE)*, 2017, pp. 1–4.

[46] C. H. Huang, H. Gao, G. B. Torri, S. Mao, Y. Jeong, D. Cheyns, V. Rochus, and X. Rottenberg, "Design, modelling, and characterization of display compatible pmut device," in *2018 19th International Conference on Thermal, Mechanical and Multi-Physics Simulation and Experiments in Microelectronics and Microsystems (EuroSimE)*, 2018, pp. 1–4.

[47] H. Yang, M. Ji, X. Xiu, H. Lv, A. Gu, and S. Zhang, "Alscn film based piezoelectric micromechanical ultrasonic transducer for an extended long-range detection," *Micromachines*, vol. 13, no. 11, 2022.

[48] Y. Kusano, I. Ishii, T. Kamiya, A. Teshigahara, G.-L. Luo, and D. A. Horsley, "High-spl air-coupled piezoelectric micromachined ultrasonic transducers based on 36% scaln thin-film," *IEEE Transactions on Ultrasonics, Ferroelectrics, and Frequency Control*, vol. 66, no. 9, pp. 1488–1496, 2019.

[49] "Piezo-micro-ultrasound-transducers for air-coupled arrays: Modeling and experiments in the linear and non-linear regimes," *Extreme Mechanics Letters*, vol. 40, p. 100968, 2020.

[50] N. Arora, P. Singh, R. Kumar, R. Pratap, and A. Naik, "Mixed nonlinear response and transition of nonlinearity in a piezoelectric membrane," *ACS Applied Electronic Materials*, vol. 6, no. 1, pp. 155–162, 2024.

[51] Z. Luo, J. Cai, S. Zhang, Y. Gu, L. Lou, and T. Wu, "Nonlinearity of piezoelectric micromachined ultrasonic transducer using aln thin film," *IEEE Open Journal of Ultrasonics, Ferroelectrics, and Frequency Control*, vol. 2, pp. 96–104, 2022.

[52] L. Evans and H. Bass, "Tables of absorption and velocity of sound in still air at 68 °f," *Wyle Laboratories, Report WR72-2*, 1972.